

Morphological Autocorrelation Transform: A New Representation and Classification Scheme for Two-Dimensional Images

Alexander C. P. Loui, *Member, IEEE*, Anastasios N. Venetsanopoulos, *Fellow, IEEE*, and Kenneth Carless Smith, *Fellow, IEEE*

Abstract—A methodology based on mathematical morphology is proposed for efficient recognition of two-dimensional (2-D) objects or shapes. This novel approach is based on the introduction of a shape descriptor called the morphological autocorrelation transform (MAT). The MAT of an image is composed of a family of *geometrical correlation functions* (GCF's) which define its morphological covariance in a specific direction. The MAT has a particular useful and interesting property in that it is translation, scale, and rotation invariant, although the individual GCF is direction sensitive. It is shown that in most situations, a small subset of the MAT suffices for image representation.

To establish the basis for this new area of research, the characteristics and performance of a shape recognition system based on the MAT are investigated and analyzed. Criteria for selecting a useful and effective subset of the GCF family are proposed and examined. It is found that a criterion which is based on the area under the GCF curve seems to provide promising results in terms of successful recognition. Computational complexity of the proposed morphological-based recognition system is examined. It is shown as well that important shape properties, such as area, perimeter, and orientation, are readily derived from the MAT representation. Furthermore, promising results are obtained which show that the proposed system is well suited for shape representation and classification.

I. INTRODUCTION

THERE are basically two major steps involved in shape recognition, namely feature extraction and classification. Conceptually, these steps are equivalent to the signal estimation and detection processes found in classical radar and sonar applications. However, the multi-dimensional nature of real-world objects makes the corresponding vision problem much more difficult. In general, extensions of one-dimensional (1-D) detection techniques do not necessarily work well in higher dimensional (two-, or three-dimensional (2-D or 3-D)) spaces.

The initial, and most difficult, step in the classification procedure is that of defining a set of meaningful features. The selection of meaningful features has been tradition-

ally based on the structures which human beings use in interpreting pictorial information [1]. Given that a shape descriptor has been chosen, the first step, therefore, is to represent the unknown shape using it. The chosen shape descriptor should be efficient in its use of computation, as well as faithful in providing a usable representation of the original shape. Once a feature set is established, the second step in the recognition process is the classification of the unknown shape based on the creation of a suitable measure. This usually involves the application of some criterion, such as minimum mean-square error (MMSE).

There exist a variety of representation schemes for 2-D shapes. Some examples are the chain code [2], the Fourier descriptor [3], the method of moments [4], the centroidal profile [5], and quad-tree representations [6]. Recently, the use of morphological techniques [7]–[9], for image analysis has become very popular as a consequence of the simplicity of many morphological operations. Some examples of morphological shape representation schemes are the morphological skeleton transform [10], [11], and the pattern spectrum (pecstrum) [12]–[14]. In addition, since most morphological operations are point-to-point operations (consider, for example, dilation, erosion, opening, and closing); parallel-processing techniques can be used to increase the processing speed. Correspondingly, this paper introduces a new shape representation scheme which can be implemented using simple morphological operations, and hence, is capable of providing real-time or near real-time performance for object recognition as well as for the determination of important geometrical parameters such as area, perimeter, and orientation of an image object.

Most of the aforementioned shape descriptors can be considered as first-order descriptors in the sense that only geometrical information such as boundary, area, and skeleton, is used in the representation. In this paper, a new 2-D shape representation scheme which is based on second-order geometrical information, and is related to morphological covariance, is presented and analyzed. In Section II, the definition of morphological covariance [15] is presented with some of its characteristics. On this basis, the morphological autocorrelation transform (MAT) [16] is formally defined. Basically, the MAT is composed of a family of functions which are referred to as *geometrical*

Manuscript received October 3, 1990; revised August 26, 1991.

A. C. P. Loui was with the Department of Electrical Engineering, University of Toronto, Toronto, Ont., Canada. He is now with Bell Communications Research, Red Bank, NJ 07701.

A. N. Venetsanopoulos and K. C. Smith are with the Department of Electrical Engineering, University of Toronto, Toronto, Ont., Canada M5S 1A4.

IEEE Log Number 9200283.

correlation functions (GCF's) [17]. Note that the term MAT and GCF are sometimes interchanged in this paper, as a result of the fact that a MAT can be considered to be a family of GCF's. Then, some of the characteristics of this new shape descriptor will be discussed and examined. In Section III, an integrated system is proposed which utilizes MAT for shape representation and recognition. It is shown that the MAT, or the family of GCF's, can be efficiently computed by a *morphological correlator* which is the core element of the proposed system. The computational complexity of this morphological correlator is also studied. Finally, in Section IV, the performance of the MAT as a shape descriptor is evaluated through simulation experiments.

II. SHAPE REPRESENTATION BY THE MORPHOLOGICAL AUTOCORRELATION TRANSFORM (MAT)

In this section, the mathematical definitions and properties of the MAT and its constituent elements, the GCF's are given. For this purpose, notation and terminology are first introduced.

Notation: \mathbf{R} and \mathbf{Z} are defined as the sets of real numbers and integers, respectively. We assume that the domain of an n -dimensional function f is a subset of the domain space $\mathbf{D} = \mathbf{R}^n$ or \mathbf{Z}^n . We also assume that the range of f is a subset of the range space $\mathbf{U} = \mathbf{R}$ or \mathbf{Z} . Hence, the Euclidean space \mathbf{E} is equal to the Cartesian product $\mathbf{D} \times \mathbf{U}$. Here, A , B , X , and Y are subsets of \mathbf{E} or of \mathbf{D} ; and a , b , x , and y are points in the respective sets.

The covariance basically descends from the theory of random functions of order two, and it provides a measure of the second-order properties of a signal. The structuring element in this case is a pair of points separated by a certain distance and positioned at a certain angle. More specifically, in morphological terms, the covariance is defined, as in [18], [15], to be the measure of the eroded set by the structuring element B which consists of a pair of points separated by a distance equivalent to the amount of spatial shift, h , at an angle ϕ .

Let X be a deterministic compact set in \mathbf{R}^n , with the structuring element, $B^\phi = \{0, h\}$, composed of two single points separated by a distance h at an angle ϕ relative to 0° . The morphological covariance $C(h)$ is defined [15] as the measure of the set $X \ominus B^\phi$, which is X eroded by B^ϕ . If we consider the translation B_x^ϕ of B by x at an angle ϕ , point x belongs to the eroded set $X \ominus B$ iff x and $x + h \in X$. Hence:

$$X \ominus B^\phi = X \cap X_{-h}^\phi. \quad (1)$$

The covariance $C(h)$ is given by¹

$$C(h) = \text{Mes}[X \ominus B^\phi] = \int_{\mathbf{R}^n} c(x) c(x + h) dx \quad (2)$$

¹Notice that the "two-point" structuring element is an effective way of computing the morphological covariance. A similar "line" structuring element used in linear erosion does not produce the same result when dealing with nonconvex shapes.

where $\text{Mes}[X]$ is the Lebesgue measure of X , and $c(x)$ is the indicator function associated with the set X . The Lebesgue measure of X is equal to the length, area, or volume of X for $n = 1, 2$, and 3 , respectively. Hence, according to (2), the following properties of $C(h)$ can be derived:

$$C(0) = \text{Mes}[X] \quad (3)$$

$$C(\infty) = 0 \quad (4)$$

$$C(h) = \text{Mes}[X \ominus B^\phi] = \text{Mes}[X \ominus B^{\phi \pm \pi}] = C(-h) \quad (5)$$

$$C(h) \leq C(0). \quad (6)$$

Note that the notions of global covariance and variogram can be applied to any random set. In this case, let X be a compact random set. Then the covariance $C(h)$ is

$$\begin{aligned} C(h) &= E \left[\int_{\mathbf{R}^2} c(x) c(x + h) dx \right] \\ &= \int_{\mathbf{R}^2} E[c(x) c(x + h)] dx \end{aligned} \quad (7)$$

where $c(x)$ is the indicator function associated with X , and the expectation is taken with respect to the random variable h . Thus

$$C(h) = \int P\{x, x + h \in X\} dx \quad (8)$$

where $P\{x\}$ is the probability of the event x .

A. Definition of MAT

For a continuous 2-D closed subset X of the Euclidean spaces $\mathbf{E} = \mathbf{R}^2$, the MAT² is defined as the set of GCF's:

$$K_\phi(h) \triangleq \frac{\text{Mes}[X \ominus B_h^\phi]}{\text{Mes}[Y]}, \quad 0 \leq \phi < \pi \quad (9)$$

where B_h^ϕ is the structuring element as defined above, and Y is a predefined standard binary shape (e.g., a square of size 200 by 200 pixels). For example, the MAT can be restricted to two particular directions, either vertical or horizontal. In this event, the MAT is composed of two GCF's, the vertical GCF and the horizontal GCF. The vertical GCF is defined as follows

$$K_{\pi/2}(h) = \frac{\text{Mes}[X \ominus B_1(h)]}{\text{Mes}[Y]} \quad (10)$$

where

$$B_1(h) = (1, *, \dots, *, 1)^T \quad (11)$$

and $*$ denotes "don't care" conditions. The corresponding horizontal GCF is defined as

$$K_0(h) = \frac{\text{Mes}[X \ominus B_2(h)]}{\text{Mes}[Y]} \quad (12)$$

²Though the GCF degenerates to the standard 2-D correlation for a binary image, this is, in general, not true for a gray scale image (see (14) for gray scale images).

where

$$B_2(h) = (1, *, \dots, *, 1) \quad (13)$$

i.e.,

$$\begin{aligned} B_1(0) &= (1)^T; & B_2(0) &= (1) \\ B_1(1) &= (1, 1)^T; & B_2(1) &= (1, 1) \\ B_1(2) &= (1, *, 1)^T; & B_2(2) &= (1, *, 1) \\ B_1(3) &= (1, *, *, 1)^T; & B_2(3) &= (1, *, *, 1). \end{aligned}$$

Next, the definition of the MAT is extended to gray scale images or shapes. Let f be a gray scale image signal defined on the Euclidean space $E = R^2$. Then the gray scale MAT³ is defined as the set of gray scale GCF's:

$$k_\phi(h) = \frac{Mes[f \ominus G_h^\phi]}{Mes[l]}, \quad 0 \leq \phi < \pi \quad (14)$$

where G_h^ϕ is the binary equivalent of a gray scale structuring function, \ominus represents gray scale erosion, and l is a predefined gray scale standard shape similar to Y of (9) for the case of binary input. Also, $Mes[f]$ is the Lebesgue measure of f . Note that the components of G_h^ϕ can only assume the maximum and minimum values of the gray levels used. That is, if the gray scale image function f is represented to a precision of b bits, then the two end points of $G_h^\phi(h)$ should have value equal to $2^b - 1$, with the intermediate points all equal to 0. For example, a GCF for gray scale signals can be restricted to vertical and horizontal directions as in the case of binary signals. For this situation, the vertical GCF is given by

$$k_{\pi/2}(h) = \frac{Mes[f \ominus G_1(h)]}{Mes[l]} \quad (15)$$

where

$$G_1(h) = (2^b - 1, 0, \dots, 0, 2^b - 1)^T \quad (16)$$

and the corresponding horizontal GCF is defined as

$$k_0(h) = \frac{Mes[f \ominus G_2(h)]}{Mes[l]} \quad (17)$$

where

$$G_2(h) = (2^b - 1, 0, \dots, 0, 2^b - 1). \quad (18)$$

1) *Examples:* In order to analyze some of the properties of the MAT, analytical formulas for the GCF are derived here for a few common shapes. Assume that a binary signal X , corresponding to the particular shape under study, belongs to the Euclidean space E , and the standard shape Y of (9) is equal to X . Let us begin with the first example, the rectangle shown in Fig. 1(a). Assuming that

³In this case, the equivalent of (2) is given as:

$$k(h) = \int_{R^n} f(x) f(x+h) dx$$

where $f(x)$ is the gray scale image function which is summable in R^n .

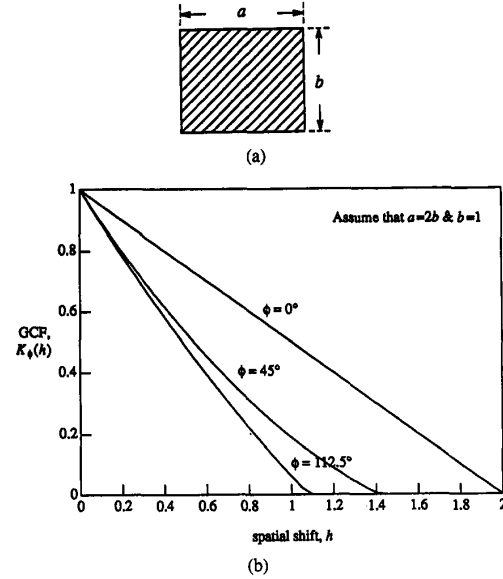


Fig. 1. (a) A binary image of a rectangle. (b) Some of its GCF's.

the amount of spatial shift is equal to h at an angle ϕ , the GCF is given by

$$K_\phi^1(h) = 1 - \left[\frac{h}{b} |\sin \phi| + \frac{h}{a} |\cos \phi| - \frac{h^2}{ab} |\cos \phi \sin \phi| \right], \quad 0 \leq \phi < 2\pi. \quad (19)$$

The derivation of the above equation can be found in Appendix A. For example, if $\phi = 0^\circ$, the GCF is simply given by $K_0^1(h) = (a - h)/a$.

Next, let us examine the example of the binary image of a disk with radius r , as shown in Fig. 2(a). Again assume a spatial shift equal to h . Since the Euclidean disk is circularly symmetric, the GCF, $K_\phi(h)$, is the same for $0 = \phi = 2\pi$. Therefore, we need only to evaluate one GCF. The GCF in this case is given by

$$K_\phi^2(h) = \begin{cases} \frac{2}{\pi r^2} \left(r^2 \cos^{-1} \frac{h}{2r} - \frac{h}{4} \sqrt{4r^2 - h^2} \right), & 0 \leq h < 2r \\ 0, & 2r \leq h. \end{cases} \quad (20)$$

The detailed derivation of this equation can be found in Appendix B. Note that it applies for $0 \leq \phi < 2\pi$; hence, it is a function of only the spatial shift h . For example, it is easily shown that $K_\phi^2(0) = 1$, $K_\phi^2(r) = (2/\pi)(\pi/2 - (\sqrt{3})/4)$, and $K_\phi^2(2r) = 0$. The GCF representing the disk, $K_\phi^2(h)$, is plotted in Fig. 2(b). Since the disk is circularly symmetric, the GCF's are the same for all directions ϕ .

The third and last example that we will consider is the binary image of an annulus. It differs dramatically from the previous examples in that it is a nonconvex shape.

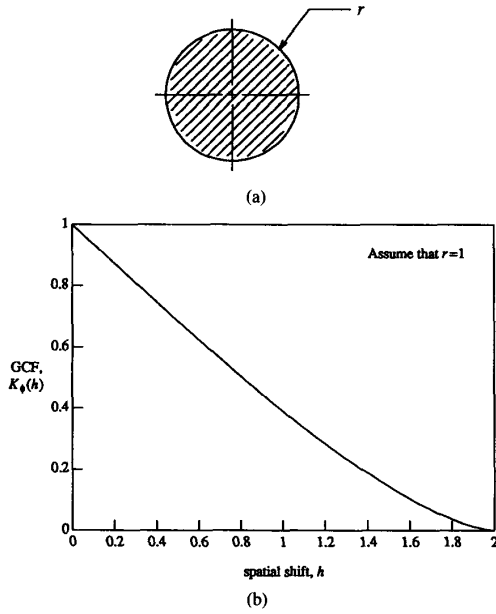


Fig. 2. (a) A binary image of a disk. (b) Some of its GCF's.

Hence, the analytical expression for the GCF is very complex. However, the annulus being circularly symmetric, its associated GCF is rotation invariant. This means that all GCF's are identical for different values of ϕ .

The annulus is depicted in Fig. 3(a) with parameters r_1 and r_2 representing the inner and outer radii, respectively. The derivation of the GCF is fairly involved, and is described in detail in Appendix C. Here, only the final expression is outlined as follows, for the case of $r_2 > 3r_1$:

$$K_\phi^3(h) = \begin{cases} \frac{S_1 - (2\pi r_1^2 - S_2)}{\pi(r_2^2 - r_1^2)}, & 0 \leq h < 2r_1 \\ \frac{S_1 - 2\pi r_1^2}{\pi(r_2^2 - r_1^2)}, & 2r_1 \leq h < r_2 - r_1 \\ \frac{S_1 - 2(\pi r_1^2 - (S_4 - S_3))}{\pi(r_2^2 - r_1^2)}, & r_2 - r_1 \leq h < r_2 \cos \theta \\ \frac{S_1 - 2(S_5 + S_3)}{\pi(r_2^2 - r_1^2)}, & r_2 \cos \theta \leq h < r_2 + r_1 \\ \frac{S_1}{\pi(r_2^2 - r_1^2)}, & r_2 + r_1 \leq h < 2r_2 \\ 0, & 2r_2 \leq h. \end{cases} \quad (21)$$

The functions $S_1, S_2, S_3, S_4,$ and S_5 are described by the following equations:

$$S_1 = 2 \left(r_2^2 \cos^{-1} \left(\frac{h}{2r_2} \right) - \frac{h}{4} \sqrt{4r_2^2 - h^2} \right) \quad (22a)$$

$$S_2 = 2 \left(r_1^2 \cos^{-1} \left(\frac{h}{2r_1} \right) - \frac{h}{4} \sqrt{4r_1^2 - h^2} \right) \quad (22b)$$

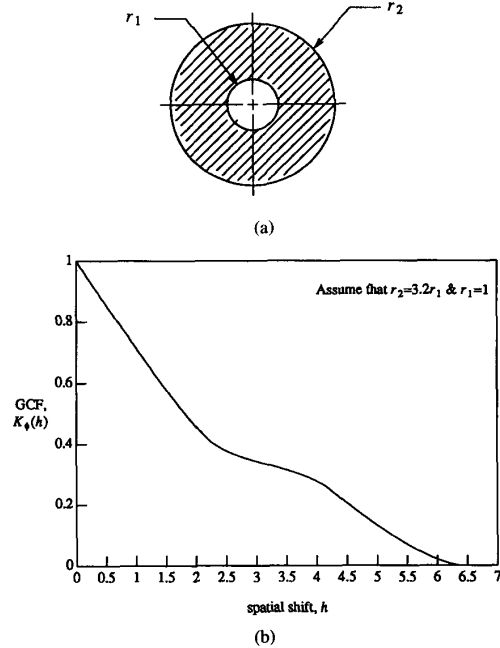


Fig. 3. (a) A binary image of an annulus. (b) Some of its GCF's.

$$S_3 = \frac{r_2^2}{2} (2\theta - \sin 2\theta) \quad (23a)$$

$$S_4 = \frac{r_1^2}{2} (2\beta - \sin 2\beta) \quad (23b)$$

$$S_5 = \frac{r_1^2}{2} (2\alpha - \sin 2\alpha) \quad (23c)$$

where

$$\theta = \cos^{-1} \left(\frac{h^2 + r_2^2 - r_1^2}{2hr_2} \right) \quad (24a)$$

$$\begin{aligned}\beta &= \sin^{-1} \left(\frac{r_2}{r_1} \sin \theta \right) \\ &= \sin^{-1} \left(\frac{r_2 (4h^2 r_2^2 - (h^2 + r_2^2 - r_1^2)^{1/2})}{2hr_2} \right)\end{aligned}\quad (24b)$$

and

$$\alpha = \beta. \quad (24c)$$

The GCF ($K_\phi^3(h)$) of the annulus is plotted in Fig. 3(b). Note that the width of the horizontal platform in the graph is approximately equal to the difference of the two radii, r_2 and r_1 .

From these examples, it can be observed in general that the complexity associated with the analytical expression of the GCF increases drastically for nonconvex shapes. Also, it is apparent that the formula for a curved shape is usually more complicated than that for a polygonal shape.

B. Properties of MAT

In this section, some of the global properties of the GCF family are examined. One concerns an interesting relationship between the *envelope* of the GCF and that of the GCF generated by the convex hull of the shape. This relationship will be demonstrated by considering the GCF of the binary shape shown in Fig. 4. Since this shape is nonconvex, one would expect a subfamily of its GCF's not to be smooth functions. In fact, generally speaking, if the input shape possesses repeated structures, the corresponding GCF will also exhibit some degree of periodicity. Here, we will call this kind of shape *pseudoperiodic* and the corresponding GCF a *pseudoperiodic* GCF.

In Fig. 4, two GCF's of the nonconvex structure X are depicted. The one for $\phi = 0^\circ$ is indicated by the solid line and the one for $\phi = 90^\circ$ is indicated by the dotted line. In particular, $K_0(h)$ possesses three local maxima due to the periodic nature of X . The *envelope* of the GCF at $\phi = 0^\circ$ can be found by connecting the points of local maximum of $K_0(h)$ together. This is represented by the short-dashed line in Fig. 4(b).

Now let us consider the GCF of the convex hull, $K_\phi^H(h)$, of the structure X . This is simply a rectangle with dimensions $(2b + a) \times a$. Hence, $K_0^H(h)$ is equivalent to $K_\phi^H(h)$ given in the example for a rectangle. This is represented by the long-dashed line in Fig. 4(b) and is given by the following equation:

$$K_0^H(h) = \frac{2b + a - h}{2b + a}. \quad (25)$$

Now assuming that $b > 2a$ in the structure of Fig. 4(a), then, it can be shown that $K_0(0) = 1$, $K_0(b) = 2/3$, and $K_0(2b) = 1/3$. The corresponding values for the GCF of the convex hull can be obtained by substituting the appropriate values in (25). Thus we have $K_0^H(0) = 1$, $K_0^H(b) = (b + a)/(2b + a)$, and $K_0^H(2b) = a/(2b + a)$. The slope of *envelope* can be obtained readily and is given by $m = 1/(3b)$. Hence, the GCF of the convex hull of the struc-

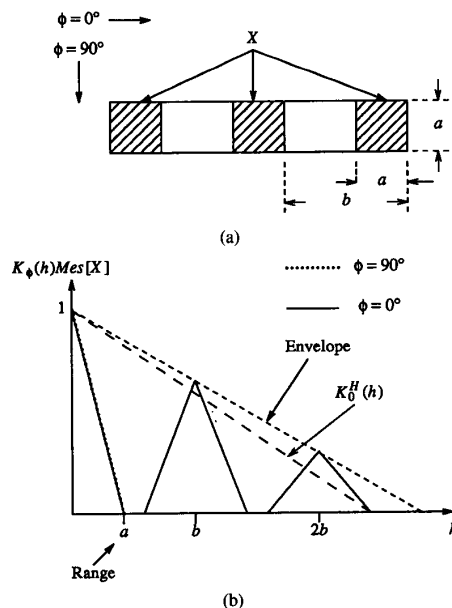


Fig. 4. (a) A binary structure X . (b) Two of its GCF's (K_0 , $K_{\pi/2}$).

ture X can be determined from $K_\phi(h)$ and a scaling factor F . The scaling factor F can be determined from the spatial shift, h , at which $K(h) = 0$, that is, in this case:

$$F = \frac{2b + a}{3b}. \quad (26)$$

For example, if $h = b$, $K_0(h) = 2/3$, then the equivalent spatial shift for $K_0^H(h)$ is given by $h' = (2b + a)/3$. Substituting this value into (25) yields $K_0^H(h') = 2/3$, which is what is expected. Hence, we can see, in general, that the *envelope* of the GCF's of a nonconvex shape is related to the global or macrostructure of the shape under study. In addition, the *range* of the GCF in the direction ϕ is defined as the smallest a such that $K_\phi(h) = 0$. Thus the *range* can also provide an indication of the local geometry of a shape.

Next, we will investigate some of the basic properties of the MAT or GCF as a shape descriptor. These include possible invariance under translation, rotation, and scale change. As the case for other shape descriptors, these characteristics are important attributes, of which one should be aware when using the MAT for shape description.

Property 1: The MAT of a signal is not in general unique to that signal.

Since the MAT contains only second-order information of a 2-D signal, the original signal cannot, in general, be recovered solely from the GCF. The GCF can be classified then as a noninformation preserving shape descriptor.

Property 2: The GCF is an even positive valued function.

That the GCF is an even positive valued function is quite obvious, since the GCF's evaluated at direction ϕ and at direction $\phi \pm \pi$ are the same.

Property 3: The maximum value of the GCF occurs at the origin, i.e., $K(0) \geq K(h)$.

This is the direct consequence of Property 2.

Property 4: The GCF is invariant under signal translation.

This follows since computing the GCF is a morphological operation.

Property 5: A single GCF is not invariant under signal rotation. However, the family of GCF's, or equivalently the MAT, is rotation invariant.

This is obvious because the GCF (as defined in (9)) is direction dependent.

Property 6: The GCF is not in general invariant under signal scale change. However, with some normalization, the GCF can be made scale invariant.

Property 7: The area of the shape can be derived from its GCF directly as

$$\text{Area}[X] = K_\phi(0) \times \text{Area}[Y]. \quad (27)$$

Property 8: The perimeter of the shape can be derived from its GCF's as [15], [16]:

$$\text{Per}[X] = -\frac{\text{Area}[Y]}{2} \int_0^{2\pi} \left. \frac{\partial K_\phi(h)}{\partial h} \right|_{h=0} d\phi. \quad (28)$$

1) *Examples:* Some examples are given to illustrate the application of some of the properties listed above. First, consider the case of the binary image of a rectangle as shown in Fig. 1(a) and its GCF as given in (19). We want to obtain its perimeter by using *Property 8*, which provides a relationship between the derivative of the GCF at the origin and the perimeter of the original shape. Hence, according to (28), the perimeter of the rectangle can be obtained from the following equation:

$$\text{Per}^1[X] = \frac{ab}{2} \left\{ 4 \int_0^{\pi/4} \left. \frac{\partial K_\phi^1(h)}{\partial h} \right|_{h=0} d\phi \right\} \quad (29)$$

where

$$\frac{\partial K_\phi^1(h)}{\partial h} = -\frac{\cos \phi}{a} - \frac{\sin \phi}{b} + \frac{2h \cos \phi \sin \phi}{ab}. \quad (30)$$

Now substituting $h = 0$ into (29), and then evaluating the integral (28) yields

$$\text{Per}^1[X] = -\frac{ab}{2} 4 \left[-\frac{1}{a} - \frac{1}{b} \right] = 2(a + b) \quad (31)$$

which is the expected result.

Following the same procedure, the perimeter of the disk in Fig. 2(a) can be derived. This is outlined as follows:

$$\text{Per}^2[X] = -\frac{\pi r^2}{2} \int_0^{2\pi} \left. \frac{\partial K_\phi^2(h)}{\partial h} \right|_{h=0} d\phi \quad (32)$$

where

$$\begin{aligned} \frac{\partial K_\phi^2(h)}{\partial h} &= \frac{2}{\pi r^2} \left[-\frac{r}{2} \frac{2r}{\sqrt{4r^2 - h^2}} \right. \\ &\quad \left. - \left(\frac{1}{4} \sqrt{4r^2 - h^2} - \frac{h^2}{4} \frac{1}{\sqrt{4r^2 - h^2}} \right) \right] \\ &= \frac{2}{\pi r^2} \left[\frac{-4r^2 + h^2}{2\sqrt{4r^2 - h^2}} \right]. \end{aligned} \quad (33)$$

Hence, setting $h = 0$ in (33), substituting it into (32), and carrying out the integration, yields

$$\text{Per}^2[X] = -\frac{\pi r^2}{2} \int_0^{2\pi} \frac{-2}{\pi r} d\phi = 2\pi r \quad (34)$$

which agrees with the expected value.

III. SYSTEM DESIGN FOR SHAPE RECOGNITION

A. System Description

In this section, a practical shape analysis system based on the MAT is presented. Its block diagram is shown in Fig. 5. In this paper, we assume that the sensed information is an image which corresponds to the 2-D projection of a 3-D real object. The first step is the acquisition of the input signal. After acquisition, the incoming signal is digitized through an A/D converter and then applied to the preprocessing module. The preprocessing module will then provide facilities for enhancement and restoration of the digitized image.

The next step towards object identification is segmentation. Segmentation is a technique that partitions an image into disjoint regions. Various methods can be used for segmentation, such as thresholding, edge detection, and region growing. After segmentation, the region of interest is located and the main task of feature extraction follows.

The next three steps in Fig. 5 relate to the major tasks of feature extraction and description. These tasks are carried out using the geometrical correlation functions proposed in Section II. If we want the system to be size invariant, the object or shape to be described must be prescaled before computing its MAT. To accomplish this, the 2-D signal representing the unknown object is linearly and isotropically scaled along the two mutually perpendicular coordinate axes, so that the resulting measure is equal to a predefined standard measure or M_s . One scale factor which provides such a transformation for an area measure can be computed as follows:

$$s = \left\{ \frac{M_s}{\text{Area}[X]} \right\}^{1/d} \quad (35)$$

where d is equal to n for a n -D binary signal. However, this section can be by-passed if size invariance is not needed. This option is clearly useful if, for example, we want to detect similar objects of different sizes.

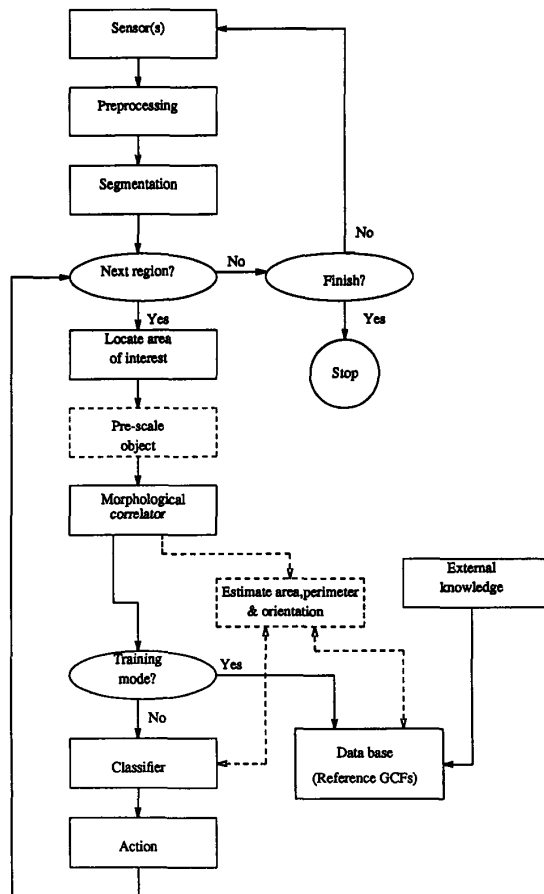


Fig. 5. An integrated morphological shape analysis system.

The next step in the block diagram of Fig. 5 is the morphological correlator. In this module, the MAT (or the family of GCF's) is computed and a subfamily of representative feature functions is selected according to some criteria such as maximum or minimum area under the curve. The selection of different criteria will be discussed in a later section. The GCF's that we obtain from the morphological correlator can provide us with information regarding geometrical properties of the unknown object or shape. For example, as noted, both the area and perimeter can be deduced from the GCF's. In addition, the orientation of the unknown shape can be estimated from the identities of the GCF's. This step is optional if the only objective of the system is to identify the object. The operation of the *morphological correlator* and the related estimation processes are described in greater depth in the next section.

The second-last module is the classifier. The purpose of the classifier is to decide which object is present based on the attributes of the unknown object relative to those of the reference set. During the classification step, the descriptor values from each of the segmented regions are compared and matched with the reference values, with classification made according to some decision rules. In

here, a deterministic classifier based on the minimum distance criterion is adapted. A statistical classifier such as the one based on the Neyman-Pearson criterion may also be used if the statistical properties of the various shapes are known.

Finally, the outcome of the classifier is passed on to the last module which performs an action such as sending a feedback signal to a robot, or activating some other device.

B. Morphological Correlator

The *morphological correlator* is the heart of the proposed object identification system. Its block diagram is shown in Fig. 6. The basic structure consists of m parallel computation units which we label gcf_0 to gcf_{m-1} , and a feature selection unit. The m parallel units compute the GCF of the unknown 2-D image signal for m different directions. The feature selection unit selects a small subset, m_f where $m_f \ll m$, among the m functions based on some predefined criterion. Note that the value of m_f is related to the probability of misclassification. A smaller m_f implies a more efficient representation, but one having a higher probability of misclassification.

One feature subset is based on the maximum and/or minimum area under the family of GCF's of a given object. The area under the GCF provides an indication of the geometrical symmetry of an object, i.e., the smaller the area, the bigger the change in correlation as the object is moved. This in turn implies that the dimension of the object in one direction is relatively smaller than that in the other. Other criteria, such as the slope at the origin of the GCF and/or the number of slope changes, can also be used. For the experiments presented in Section IV, the criterion based on the area under the GCF is used due to its simplicity of implementation.

Finally, geometrical information which might be useful for classification or decision making, such as area, perimeter, and orientation of the unknown input shape, can be obtained if necessary. This is done by using the GCF's available from the *morphological correlator* in correspondence to the operations indicated by the dashed box of Fig. 5. Specifically, the area and perimeter of the unknown shape can be determined from (27) and (28), respectively. The orientation of the unknown object can be estimated from the angle associated with an individual GCF. This is done by comparing the angles associated with the corresponding reference object's GCF and those of the rotated and translated object's GCF. For example, a square rotated by 45° will result in a GCF evaluated at 0° , that looks like the GCF for the reference square evaluated at 45° . Hence, differences between the angles associated with the two GCF's of the same shape give an indication of the orientation of the unknown object.

C. Computational Complexity

In this section, the computational complexity of the proposed shape descriptor based on the MAT is examined. Specifically, we will look at the complexity of the

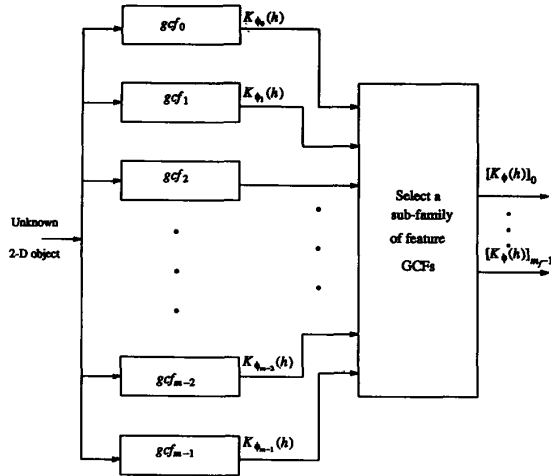


Fig. 6. Block diagram of the morphological correlator.

morphological correlator as well as of the related geometrical parameter estimation processes. These analyses will provide us with an idea of the implementation complexity involved, and thus of the potential implementation cost.

Let us begin with the *morphological correlator* of Fig. 6. The parameter m represents the number of GCF's to be evaluated; and m_f represents the number of feature GCF's that will be used for classification or recognition. Obviously, the smaller the m_f , the less the computation requirement. This reduction, however, might come at the expense of a higher probability of misclassification due to inadequate representation of the original MAT. Hence, there is a trade-off between the complexity of the *morphological correlator* and the performance of the resulting recognition system. However, more work needs to be done to quantify the trade-offs involved.

Here, the computation time or cycle time will be used to measure the computational complexity involved in the calculation of the GCF's. For the following analysis, we assume that the GCF's are computed using the hit-and-miss transformation [15]. This implies that erosion is realized by fitting the two-point structuring elements into the input image, and probing the relation of the image relative to the structuring elements. Hence, the types of operations involved are comparisons, logical operations (AND), additions, and multiplications (for scaling and normalization). The definitions of the parameters used in the analysis are given as follows:

m	Number of GCF's.
m_f	Number of feature GCF's.
N_m	Length of GCF.
$M \times N$	Image size (rows \times columns).
$(M - M_{ij}) \times (N - N_{ij})$	Region of support.
N_{cp}	Number of comparisons.
N_{lp}	Number of logical operations.

N_{ad}	Number of additions.
N_{mu}	Number of multiplications.
T_{cp}	Comparison time.
T_{lp}	Logical operation time.
T_{ad}	Addition time.
T_{mu}	Multiplication time.

According to Fig. 6, the front end of the *morphological correlator* consists of m parallel units each computing the GCF in a particular direction. The cycle time of each of these units is

$$C_{li} = N_{cp}^{li} T_{cp} + N_{lp}^{li} T_{lp} + N_{ad}^{li} T_{ad} + N_{mu}^{li} T_{mu} \quad (36)$$

where

$$N_{cp}^{li} = 2 \sum_{j=0}^{N_m-1} (M - M_{ij})(N - N_{ij}) \quad (37a)$$

$$N_{lp}^{li} = N_{ad}^{li} = \sum_{j=0}^{N_m-1} (M - M_{ij})(N - N_{ij}) \quad (37b)$$

$$N_{mu}^{li} = 2. \quad (37c)$$

The second stage of the *morphological correlator* consists of a feature selection unit where a subfamily of feature GCF's is selected based on a predefined criterion. Assume that the criterion based on the area under the GCF curve is used, as described in the previous section. Correspondingly, the types of operations involved are basically addition and sorting. The processing time C_2 is given by

$$C_2 = N_{ad}^2 T_{ad} + N_{st}^2 T_{st} \quad (38)$$

where

$$N_{ad}^2 = m_f(N_m - 1) \quad (39a)$$

$$N_{st}^2 = 1. \quad (39b)$$

There are basically two different scenarios depending on whether the m units are implemented in series or in parallel. For a serial implementation, the processing time is

$$C_s = \sum_{i=1}^m C_{li} + C_2 \quad (40)$$

and for parallel implementation, it is given by

$$C_p = \max_i \{C_{li} + C_2\}, \quad 0 \leq i < m. \quad (41)$$

By way of example, assume that $m = 8$, with the following angular representations: $\phi_0 = 0$, $\phi_1 = \pi/6.77$, $\phi_2 = \pi/4$, $\phi_3 = \pi/2.84$, $\phi_4 = \pi/2$, $\phi_5 = \pi/1.54$, $\phi_6 = (3\pi)/4$, and $\phi_7 = \pi/1.17$. Note that these angles are chosen to correspond to the integer-grid coordination of the image signal, e.g., $\phi_1 = \tan^{-1}(1/2) = \pi/6.77$ and $\phi_3 = \tan^{-1} 2 = \pi/2.84$. Hence, the parameters M_{ij} and N_{ij} of the region of support for each of the GCF's are

given as follows:

$$\begin{aligned} M_{0j} &= 0; & M_{1j} &= M_{7j} = j; & M_{2j} &= M_{6j} = j; \\ M_{3j} &= M_{5j} = 2j; & M_{4j} &= j; \\ N_{0j} &= j; & N_{1j} &= N_{7j} = 2j; & N_{2j} &= N_{6j} = j; \\ N_{3j} &= N_{5j} = j; & N_{4j} &= 0. \end{aligned}$$

Substituting these values into (37) and then (40) yields

$$\begin{aligned} C_s &= \left\{ 8N_m MN - \frac{9}{2}(N_m)(N_m + 1)(M + N) \right. \\ &\quad \left. + 10 \sum_{j=0}^{N_m-1} j^2 \right\} [2T_{cp} + T_{lp} + T_{ad}] \\ &\quad + 2N_{mu} T_{mu} + m_f(N_m - 1)T_{ad} + T_{st}. \end{aligned} \quad (42)$$

If the m units can be implemented in parallel, the computation time can be greatly reduced. Otherwise, according to (36), (38), and (41), the computation time C_p is given by

$$\begin{aligned} C_p &= \max_i \left\{ \sum_{j=0}^{N_m-1} (M - M_{ij})(N - N_{ij}) \right. \\ &\quad \left. \cdot (2T_{cp} + T_{lp} + T_{ad}) + 2T_{mu} \right\} \\ &\quad + (N_m - 1)T_{ad} + T_{st}, \quad 0 \leq i < m. \end{aligned} \quad (43)$$

Substituting the M_{ij} 's and N_{ij} 's, and simplifying, yields

$$\begin{aligned} C_p &= [N_m MN - N_m(N_m + 1)M][2T_{cp} + T_{lp} + T_{ad}] \\ &\quad + 2T_{mu} + (N_m - 1)T_{ad} + T_{st}. \end{aligned} \quad (44)$$

Hence, the computation involved in calculating the GCF is substantial. This is especially true for the case of serial implementation and/or where M and N are large.

In short, it can be concluded that the major bottleneck in a recognition system based on the idea of GCF's is on the computation of the GCF's themselves. One possible solution to this problem is to compute the GCF's using a dedicated high-speed architecture. The problem of efficient and real-time implementation of morphological operations, and in particular, the *morphological correlator*, is addressed in another paper [19].

IV. PERFORMANCE EVALUATION

In this section, the performance of the MAT as a shape descriptor is examined by simulation. Experiments were conducted using twelve different shapes as shown in Figs. 7-9. These shapes were chosen to cover a wide range of practical objects. The reference MAT of each shape is shown in Figs. 14-25 of Appendix D.

In each graph, each GCF of the MAT is identified in the upper-right legend, in order of increasing slope, where slope is defined here as the slope of the GCF curve at the origin. For example, in Fig. 17, there are only three curves, so according to the legend, the first curve actually represents two GCF's: gcf_0 (0°) and gcf_4 (90°). The sec-

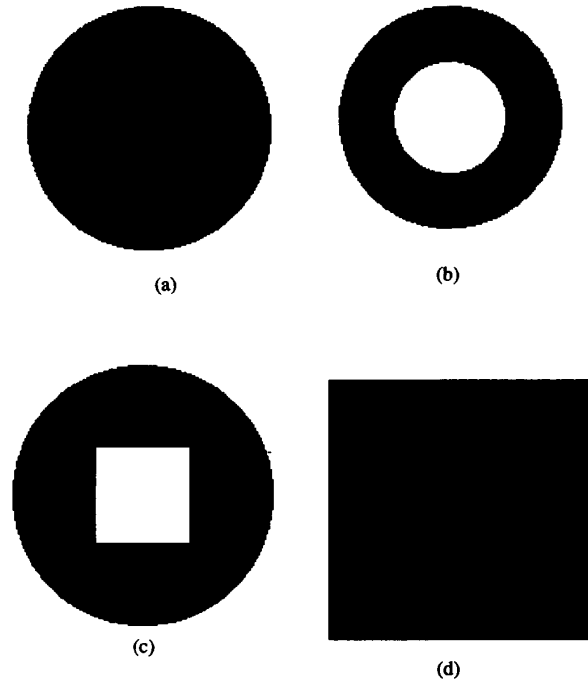


Fig. 7. Binary test images. (a) Disk. (b) Annulus. (c) Socket. (d) Square.

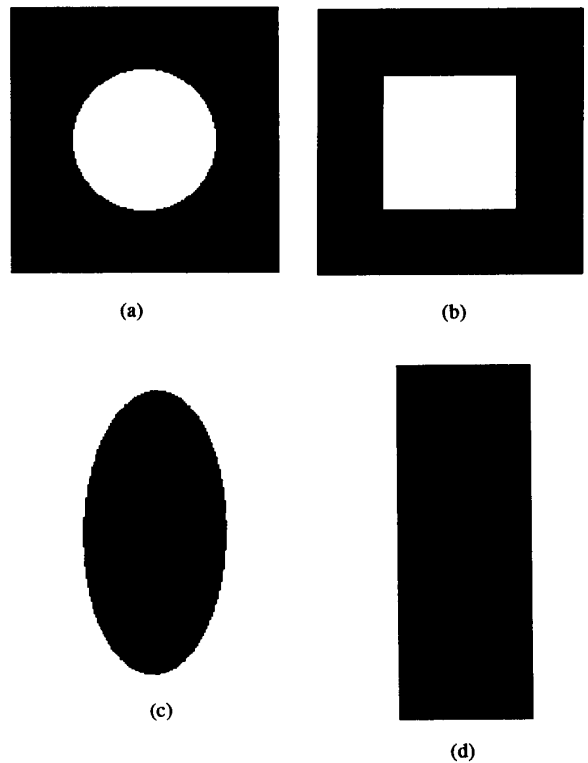


Fig. 8. Binary test images. (a) Nut. (b) Frame. (c) Ellipse. (d) Rectangle.

ond curve is the coincidence of four GCF's: gcf_1 , gcf_3 , gcf_5 , and gcf_7 . Then gcf_2 coincides with gcf_6 to form the last curve. The number of different curves in each graph

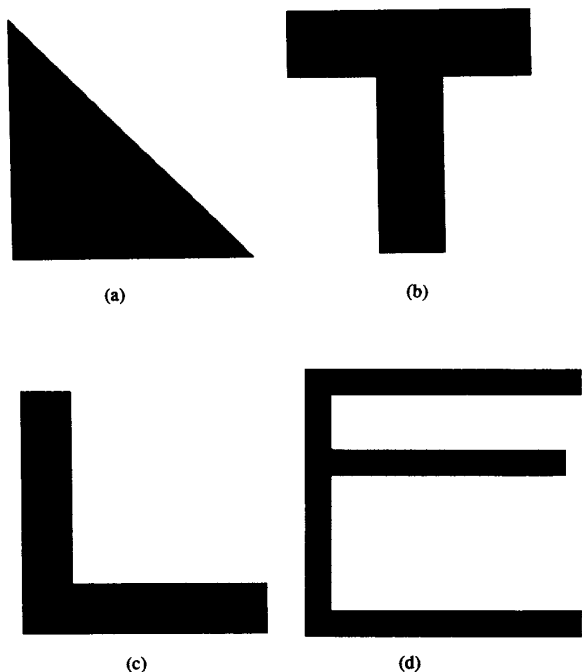


Fig. 9. Binary test images. (a) Triangle. (b) T. (c) Angle. (d) E.

gives an indication of the degree of object symmetry. That is, the fewer the number of distinct curves, the more symmetrical the object. Hence, among the 12 test objects, the *disk* and the *annulus* are the most symmetrical objects, whereas the *angle* and the *E* can be seen to be the most nonsymmetrical.

A. Geometrical Interpretation

Next, we will examine correspondences between the actual geometry of the shape and its MAT. Fig. 14 shows the graphs of MAT of the reference object *disk*. Since the object *disk* is circularly symmetric, the shape of the MAT, $K_\phi(h)$, is independent of the angle ϕ . In fact, this particular object is rotation invariant by nature. Note that the object *annulus* is also rotation invariant. The difference between the *disk* and the *annulus* is that the slope of the *disk*'s GCF is fairly constant, whereas it levels off between $h = 40$ and $h = 90$ for the *annulus* as shown in Fig. 15. This is due to the fact that the area of overlap at that range of spatial shifts is fairly constant for the *annulus*. Now consider the test object *socket* which is depicted in Fig. 16. The *socket* is basically a circular disk with a square opening in the center. Since the shape of *socket* is very similar to that of the *annulus*, we will expect the MAT of the two to be also very similar. This indeed is the case as we compare Figs. 15 and 16. The fact that object *socket* has a square opening in the center causes its GCF to be less smooth than that of the *annulus*. This effect is more pronounced when we look at the MAT for the object *square* shown in Fig. 17. From Fig. 17, it

can be seen that three distinct GCF's exist for the *square*, which is the reason why Fig. 16 also exhibits three distinct curves. In fact, Fig. 16 can be considered as the "superposition" (in a second-order sense) of Figs. 15 and 17. Next, the GCF's of the *nut*-shaped object of Fig. 8(a) are shown in Fig. 18. Again, there is close resemblance between Figs. 18 and 15. Fig. 18 can also be considered as the "superposition" of Fig. 15 and Fig. 17, except in this case Fig. 17 (the MAT of *square*) is the dominant one, whereas for the object *socket* (Fig. 16) Fig. 15 (the MAT of *annulus*) is the dominant one. Fig. 19 shows the GCF's of the object *frame* which is very similar to that of the object *nut* (Fig. 18). Again, this is expected since the only difference between the two objects is the shape of the central opening. The one with a circular center will obviously produce a GCF with slope transitions that are smoother than the one with a square center.

Up to now, we have examined the six most symmetric test objects and their respective GCF's. Generally speaking, as noted, it can be observed that the number of distinct GCF's relates to the symmetry of the object and the GCF of a particular object can be deduced from objects with similar geometry. Next, we will examine the remaining (more complex) test objects and their corresponding GCF's. Figs. 20–22 show the GCF's for the objects *ellipse*, *rectangle*, and *triangle* (Figs. 8(c), (d), and 9(a)), respectively. These three objects can be considered as belonging to the same class in the sense that each possesses some form of half symmetry. Thus the number of distinct curves in each case is the same and is equal to five.

The final set of test objects is comprised of three nonconvex objects. These are the *T*, the *angle* and the *E* as depicted in Fig. 9(b)–(d), respectively. The GCF's of these shapes are shown in Figs. 23–25, respectively. The GCF's of this type (nonconvex) of object are usually not smooth and fairly complicated due to the overlapping of different components during shifting. This is especially obvious for the object *E* as indicated by the GCF's in Fig. 25. In Fig. 25, gcf_4 corresponds to spatial shifting at an angle $\phi = 90^\circ$, and three peaks are found at $h = 50$, $h = 100$, and $h = 150$. This implies that there exists some form of periodicity within the object under investigation. These three local peaks, in fact, correspond to the overlapping effect of the three horizontal bars of the object *E* with each other. This characteristic also appears in several other GCF's in Fig. 25. The variation from one GCF to another is reasonable, since at different angles ϕ , the amount of overlap (and hence, the amplitude and the location of the peaks) will be different. This is illustrative of the fact that the GCF can provide us with information relating to the local structure of an object.

B. Simulation Results

Experiments have been carried out to study the performance of the MAT for 2-D object classification. The twelve reference shapes discussed earlier were arbitrarily

TABLE I
CONFUSION MATRIX FOR 12 DIFFERENT SHAPES USING ONLY THE MAXIMUM FEATURE FUNCTION

Euclidean Distances ($\times 10$) from Translated and Rotated Shapes to Reference Shape Set												
Shape	disk	annulus	socket	square	nut	frame	ellipse	rect	tri	T	angle	E
disk	0.00	19.34	3.39	25.42	4.16	3.34	6.10	8.53	5.59	12.53	23.47	13.66
annulus	19.38	0.00	8.48	86.15	24.97	18.99	4.80	38.19	4.64	0.94	0.43	0.97
socket	3.40	8.46	0.00	41.87	4.99	2.65	2.19	13.67	1.63	4.18	11.47	5.53
square	29.10	92.45	46.42	0.15	24.05	30.43	57.55	16.85	57.19	76.16	100.82	78.81
nut	4.13	24.88	4.94	21.19	0.00	0.47	10.45	4.12	10.06	16.81	29.15	18.77
frame	3.59	21.55	3.65	24.27	0.19	0.09	8.37	4.84	7.97	13.99	25.38	15.78
ellipse	5.91	5.09	2.12	51.75	10.06	6.73	0.01	16.98	0.14	2.01	6.71	2.00
rect	14.65	49.05	21.05	13.74	7.84	10.71	25.58	0.86	25.91	37.64	53.51	38.49
tri	4.73	6.85	1.56	46.51	7.58	4.77	0.37	13.27	0.40	2.99	8.72	3.16
T	10.70	1.45	3.33	65.98	15.06	10.49	1.14	25.45	0.98	0.09	2.58	0.35
angle	19.83	0.30	9.18	86.45	25.27	19.25	4.39	37.27	4.49	1.03	0.21	0.65
E	10.55	3.45	4.04	61.42	13.22	9.29	0.84	20.51	1.16	1.38	4.26	1.03
Decision Correct?	yes	yes	yes	yes	yes	yes	yes	yes	no	yes	yes	no

TABLE II
CONFUSION MATRIX FOR 12 DIFFERENT SHAPES USING ONLY THE MINIMUM FEATURE FUNCTION

Euclidean Distances ($\times 10$) from Translated and Rotated Shapes to Reference Shape Set												
Shape	disk	annulus	socket	square	nut	frame	ellipse	rect	tri	T	angle	E
disk	0.00	19.24	3.54	20.18	5.94	6.65	19.14	7.85	15.46	17.11	34.41	35.79
annulus	19.26	0.00	8.05	75.90	13.43	9.85	1.36	8.65	1.38	0.56	2.62	2.98
socket	3.54	8.04	0.00	35.34	2.44	1.66	9.10	4.62	6.81	7.29	18.65	19.50
square	19.78	74.95	34.71	0.01	32.88	37.53	76.05	48.10	68.65	71.84	103.27	103.65
nut	6.13	12.54	2.25	34.94	0.02	0.25	11.78	4.73	9.52	10.62	22.45	24.11
frame	7.42	9.16	1.87	40.77	0.51	0.14	8.88	4.24	6.98	7.69	17.71	19.02
ellipse	18.85	1.39	8.93	76.43	12.36	9.44	0.00	5.04	0.20	0.27	2.88	5.19
rect	7.48	9.25	4.66	47.65	4.89	4.47	5.72	0.01	4.17	5.89	15.99	19.83
tri	16.20	1.30	7.22	71.07	10.65	7.93	0.15	4.04	0.01	0.16	3.81	5.83
T	16.46	0.71	7.16	71.63	11.28	8.31	0.31	5.06	0.14	0.04	3.39	4.86
angle	34.54	2.66	18.73	104.62	23.73	19.03	2.81	15.19	4.23	3.08	0.00	1.24
E	36.78	3.43	20.45	106.32	26.37	21.10	5.43	19.68	6.63	4.97	1.45	0.13
Decision Correct?	yes	yes	yes	yes	yes	yes	yes	yes	yes	yes	yes	yes

rotated and translated before input to the proposed recognition system of Fig. 5. Note that in most cases the rotation angle is purposely chosen not to coincide with any of the principle directions of the morphological correlator. Specifically, the amount of rotation (r) and translation (t) for each shape is as follows: *disk* (r : 170° , t : (20, 80)); *annulus* (r : 80° , t : (-100, 0)); *socket* (r : 90° , t : (-10, -70)); *square* (r : 220° , t : (-90, -90)); *nut* (r : 45° , t : (-56, 89)); *frame* (r : 300° , t : (30, -90)); *ellipse* (r : 40° , t : (50, 50)); *rectangle* (r : -33° , t : (67, -98)); *triangle* (r : 125° , t : (-30, 40)); T (r : 100° , t : (75, -60)); *angle* (r : 75° , t : (50, -90)); E (r : 50° , t : (-75, 0)).

Comparative experimental results are tabulated in the confusion matrix provided in Tables I-IV. Object scaling has not been implemented in these experiments since the system is assumed to be able to detect similar objects of different sizes. The classifier used is a simple deterministic minimum distance classifier, which in this case computes the sum of the squared distances, $d(u, r)$ between the reference GCF, $K_\phi^r(h)$ and the unknown GCF, $K_\phi^u(h)$, i.e.:

$$d(u, r) = \sum_{h=0}^{N-1} w(h) [K_\phi^u(h) - K_\phi^r(h)]^2 \quad (45)$$

where $w(h)$ is a weighting factor for the h component of the GCF, and N is the maximum extent of the GCF. The weighting factor can be chosen to put varying emphasis on different components of the GCF. The contribution of particular components can be totally eliminated by setting $w(h) = 0$. For these results, $w(h)$ is set to 1. Tables I-IV are organized in such a way that comparisons (the distance $d(u, r)$) between an unknown object and all the reference objects are listed in a column format. When all these columns are combined, a confusion matrix is formed. This allows easy examination of the performance of the proposed shape descriptor. Tables I and II list the results of detection using the maximum feature function and minimum feature function of the GCF's, respectively. In Table III, the detection results are tabulated using the sum of the maximum and minimum feature functions of the GCF's. Finally, in Table IV, the results are tabulated using the minimum of the maximum and minimum feature functions. The criterion for selecting the respective feature functions is based on the area under the GCF curve, i.e., the quantity $A[K_\phi]$, where

$$A[K_\phi] = \sum_{h=0}^{N-1} K_\phi(h). \quad (46)$$

TABLE III
CONFUSION MATRIX FOR 12 DIFFERENT SHAPES USING THE SUM OF THE MAXIMUM AND MINIMUM FEATURE FUNCTIONS

Euclidean Distances ($\times 10$) from Translated and Rotated Shapes to Reference Shape Set												
Shape	disk	annulus	socket	square	nut	frame	ellipse	rect	tri	T	angle	E
disk	0.00	38.58	6.93	45.60	10.10	9.99	25.24	16.38	21.04	29.64	57.88	49.46
annulus	38.64	0.00	16.52	162.05	38.40	28.85	6.16	46.84	6.03	1.50	3.05	3.95
socket	6.94	16.50	0.00	77.21	7.43	4.31	11.29	18.30	8.44	11.47	30.12	25.04
square	48.88	167.40	81.13	0.16	56.93	67.96	133.60	64.95	125.84	148.00	204.09	182.46
nut	10.26	37.42	7.20	56.13	0.02	0.72	22.23	8.86	19.57	27.42	51.60	42.88
frame	11.00	30.70	5.52	65.05	0.70	0.23	17.25	9.08	14.95	21.68	43.09	34.80
ellipse	24.76	6.47	11.05	128.18	22.41	16.17	0.01	22.02	0.34	2.28	9.60	7.20
rect	22.13	58.30	25.70	61.40	12.72	15.18	31.30	0.87	30.08	43.53	69.50	58.32
tri	20.93	8.15	8.78	117.58	18.23	12.70	0.53	17.32	0.41	3.16	12.53	8.98
T	27.16	2.17	10.49	137.61	26.35	18.80	1.45	30.51	1.12	0.13	5.97	5.22
angle	54.38	2.95	27.91	191.07	49.00	38.28	7.20	52.46	8.72	4.12	0.21	1.89
E	47.33	6.88	24.49	167.74	39.59	30.39	6.27	40.19	7.80	6.34	5.72	1.16
Decision Correct?	yes	yes	yes	yes	yes	yes	yes	yes	no	yes	yes	yes

TABLE IV
CONFUSION MATRIX FOR 12 DIFFERENT SHAPES USING THE MINIMUM OF MAXIMUM AND MINIMUM FEATURE FUNCTIONS

Euclidean Distances ($\times 10$) from Translated and Rotated Shapes to Reference Shape Set												
Shape	disk	annulus	socket	square	nut	frame	ellipse	rect	tri	T	angle	E
disk	0.00	19.24	3.39	20.18	4.16	3.34	6.10	7.85	5.59	12.53	23.47	13.66
annulus	19.26	0.00	8.05	75.90	13.43	9.85	1.36	8.65	1.38	0.56	0.43	0.97
socket	3.40	8.04	0.00	35.34	2.44	1.66	2.19	4.62	1.63	4.18	11.47	5.53
square	19.78	74.95	34.71	0.01	24.05	30.43	57.55	16.85	57.19	71.84	100.82	78.81
nut	4.13	12.54	2.25	21.19	0.00	0.25	10.45	4.12	9.52	10.62	22.45	18.77
frame	3.59	9.16	1.87	24.27	0.19	0.09	8.37	4.24	6.98	7.69	17.71	15.78
ellipse	5.91	1.39	2.12	51.75	10.06	6.73	0.00	5.04	0.14	0.27	2.88	2.00
rect	7.48	9.25	4.66	13.74	4.89	4.47	5.72	0.01	4.17	5.89	15.99	19.83
tri	4.73	1.30	1.56	46.51	7.58	4.77	0.15	4.04	0.01	0.16	3.81	3.16
T	10.70	0.71	3.33	65.98	11.28	8.31	0.31	5.06	0.14	0.04	2.58	0.35
angle	19.83	0.30	9.18	86.45	23.73	19.03	2.81	15.19	4.23	1.03	0.00	0.65
E	10.55	3.43	4.04	61.42	13.22	9.29	0.84	19.68	1.16	1.38	1.45	0.13
Decision Correct?	yes	yes	yes	yes	yes	yes	yes	yes	yes	yes	yes	yes

Hence, the maximum feature function, $K_{\phi_{\max}}$ is defined as

$$K_{\phi_{\max}} = \{K_{\phi}: A[K_{\phi}] \text{ is maximum}\}, \quad 0^{\circ} \leq \phi \leq 180^{\circ}. \quad (47)$$

Similarly, the minimum feature function, $K_{\phi_{\min}}$ is defined as

$$K_{\phi_{\min}} = \{K_{\phi}: A[K_{\phi}] \text{ is minimum}\}, \quad 0^{\circ} \leq \phi \leq 180^{\circ}. \quad (48)$$

From Table I, it can be observed that performance using the maximum feature function is not acceptable, as two objects are misclassified, i.e., object *triangle* is mistaken as object *ellipse*, and object E is mistaken as object T . From Table III, there is still one misclassification, as object *triangle* is recognized as object *ellipse*, again. Tables II and IV show that by using either the minimum feature function, or the minimum of maximum and minimum feature functions, all arbitrarily rotated and translated unknown objects are identified correctly. For similar, but nonidentical shapes such as *nut* and *frame* (note the similarity in Figs. 18 and 19), the results of Tables II

and IV indicate that though the Euclidean distance between the two shapes are quite small, successful classification has been achieved. Relative to the ideality of the test, it should be noted that although noise was not added explicitly to the images, there is always inherent quantization noise associated with the square grid representation of digital images. That is, it is impossible to represent an object perfectly except perhaps for simple shapes such as a square in particular proper orientations. In addition, the experiments show that the minimum feature function alone is sufficient for use in identification. One conjecture that can be made from the experimental results is that the minimum feature function is less sensitive to rotation than the maximum feature function, and, thus it is inherently more stable and reliable than the other GCF's. However, if the resolution of the angle ϕ is increased (that is if more than 8 directions are used), the performance using the maximum feature function can be expected to improve.

V. SUMMARY

In this paper, a new 2-D shape descriptor has been introduced and its performance evaluated using 12 different test objects. This shape descriptor, which we call the

MAT and its constituents, the GCF's, are based on the idea of morphological covariance and is thereby related to second-order geometrical properties of the object. In order to explore the characteristics of this new shape representation scheme, analytical formulas have been derived for a few common shapes. It has been shown that useful geometrical shape properties such as area, perimeter, and orientation of the object, may readily be derived from the MAT representation. An integrated system has been proposed which utilizes the concept of the MAT for 2-D shape recognition. Experimental results show that the MAT has great potential in shape representation and recognition of 2-D objects. Finally, a computational complexity study has shown that the computation burden of the proposed shape representation and shape recognition system lies in the computation of the MAT or the GCF family itself. Correspondingly, fast architectures has been proposed in a related paper [19] to be published separately, for possible real-time implementation of the MAT.

APPENDIX A

Consider a binary rectangle with sides of arbitrary length a and b as shown in Fig. 10(a). The GCF, $K_\phi^1(h)$ of the MAT, can be calculated by considering a spatial shift of h at an angle ϕ . The area of overlap is given by the shaded area of Fig. 10(b) and is equal to $A = (a - h \cos \phi)(b - h \sin \phi)$. Specifically, the MAT is represented by the following GCF:

$$K_\phi^1(h) = \begin{cases} \frac{(a - h \cos \phi)(b - h \sin \phi)}{ab}, & 0 \leq \phi < \frac{\pi}{2} \\ \frac{(a + h \cos \phi)(b - h \sin \phi)}{ab}, & \frac{\pi}{2} \leq \phi < \pi \\ \frac{(a + h \cos \phi)(b + h \sin \phi)}{ab}, & \pi \leq \phi < \frac{3\pi}{4} \\ \frac{(a - h \cos \phi)(b + h \sin \phi)}{ab}, & \frac{3\pi}{4} \leq \phi < 2\pi. \end{cases} \quad (\text{A.1})$$

Simplifying yields

$$K_\phi^1(h) = 1 - \left[\frac{h}{b} |\sin \theta| + \frac{h}{a} |\cos \theta| - \frac{h^2}{ab} |\cos \theta \sin \theta| \right], \quad 0 \leq \phi < 2\pi. \quad (\text{A.2})$$

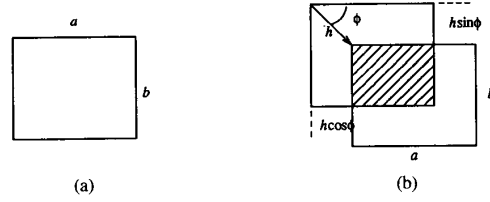


Fig. 10. (a) A binary rectangle. (b) A spatial shift of h at an angle ϕ .

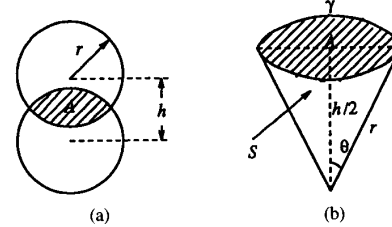


Fig. 11. (a) A binary disk shifted by h . (b) Details of the overlapped area.

APPENDIX B

The MAT of the binary disk can be determined by considering the illustrations of Fig. 11. In Fig. 11(a), the binary disk of radius r is displaced by an amount h , resulting an overlapping area A . According to Fig. 11(b), the arc length γ is given by

$$\gamma = 2r\theta = 2r \cos^{-1} \left(\frac{h}{2r} \right). \quad (\text{B.1})$$

Then the total area of the sector S is

$$S = \frac{1}{2} r\theta = r^2 \cos^{-1} \left(\frac{h}{2r} \right) \quad (\text{B.2})$$

and the overlapped area, A , is

$$\begin{aligned} A &= 2 \left(S - \left(2 \sqrt{\left(r^2 - \frac{h^2}{4} \right) \frac{h}{2}} \right) \right) \\ &= 2 \left(r^2 \cos^{-1} \left(\frac{h}{2r} \right) - \frac{h}{4} \sqrt{4r^2 - h^2} \right). \end{aligned} \quad (\text{B.3})$$

Since the binary disk is circularly symmetric in $E = \mathbf{R}^2$, the MAT does not depend on the shifting (or correlation) angle ϕ . Hence, the MAT is independent of ϕ and can be described by:

$$K_\phi^2(h) = \frac{A}{\pi r^2} = \begin{cases} \frac{2}{\pi r^2} \left(r^2 \cos^{-1} \left(\frac{h}{2r} \right) - \frac{h}{4} \sqrt{4r^2 - h^2} \right), & 0 \leq h < 2r \\ 0, & 2r \leq h. \end{cases} \quad (\text{B.4})$$

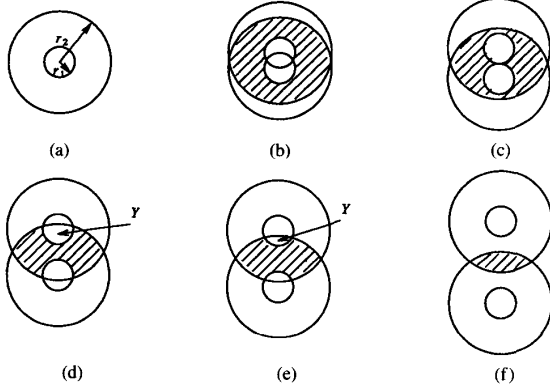


Fig. 12. (a) A binary annulus with $r_2 > 3r_1$. (b) Spatial shift of $0 \leq h < 2r_2$. (c) Spatial shift of $2r_1 \leq h < r_2 - r_1$. (d) Spatial shift of $r_2 - r_1 \leq h < r_2 \cos \theta$. (e) Spatial shift of $r_2 \cos \theta \leq h < r_2 + r_1$. (f) Spatial shift of $r_2 + r_1 \leq h < 2r_2$.

APPENDIX C

For the binary annulus of Fig. 12(a), the MAT is derived assuming that $r_2 > 3r_1$, where r_2 and r_1 are the radii of the outer and inner boundaries, respectively. The analysis is divided into six parts depending on the magnitude of the spatial shift.

1) For $0 \leq h < 2r_1$: This situation is illustrated in Fig. 12(b). Let S_1 and S_2 denote the overlapped area of the inner circles and outer circles, respectively, then the MAT is given by

$$K_\phi^3(h) = \frac{S_1 - (2\pi r_1^2 - S_2)}{\pi(r_2^2 - r_1^2)} \quad (\text{C.1})$$

where S_1 and S_2 are obtained by substituting r_2 and r_1 into (B.3) of Appendix B. That is:

$$S_1 = 2 \left(r_2^2 \cos^{-1} \left(\frac{h}{2r_2} \right) - \frac{h}{4} \sqrt{4r_2^2 - h^2} \right) \quad (\text{C.2})$$

$$S_2 = 2 \left(r_1^2 \cos^{-1} \left(\frac{h}{2r_1} \right) - \frac{h}{4} \sqrt{4r_1^2 - h^2} \right). \quad (\text{C.3})$$

2) For $2r_1 \leq h < r_2 - r_1$: In this situation, the two inner circles are embedded in the solid regions of the annulus and its shifted replica. Thus the area of overlap is simply $S_1 - 2(\pi r_1^2)$ where S_1 is the overlapped area between the two outer circles, and is given by the expression of (C.2). The expression of the MAT for this region is given by

$$K_\phi^3(h) = \frac{S_1 - 2\pi r_1^2}{\pi(r_2^2 - r_1^2)}. \quad (\text{C.4})$$

3) For $r_2 - r_1 \leq h < r_2 \cos \theta$: In this situation, the boundary of the outer circle intersects the inner circle. The cosine factor ensures that the amount of shift does not extend beyond the first half of the inner circle. This is illustrated in Figs. 12(d) and 13(a). According to Fig. 12(d), the area of overlap is given by $A = S_1 - 2Y$, where S_1 is the same as in (C.2) and Y is the partial area of the inner circle as indicated in the figure. The area Y is given

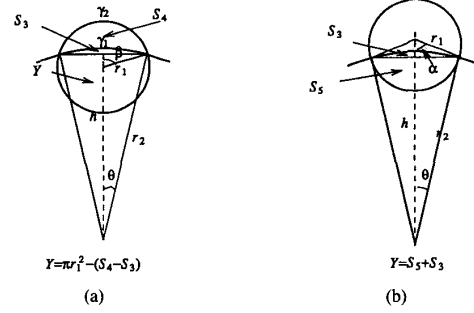


Fig. 13. (a) The geometrical relationship for the situation in Fig. 12(d). (b) The geometrical relationship for the situation in Fig. 12(e).

by

$$Y = \pi r_1^2 - (S_4 - S_3) \quad (\text{C.5})$$

where S_3 and S_4 are the areas of the sectors created by the intersection of the inside and outside boundaries as illustrated in Fig. 13(a). Thus the area S_3 is given by

$$\begin{aligned} S_3 &= \frac{1}{2} r_2 \gamma_2 - 2 \left[\frac{r_2 \cos \theta r_2 \sin \theta}{2} \right] \\ &= \frac{1}{2} r_2 (2r_2 \theta) - r_2^2 \sin \theta \cos \theta \\ &= \frac{r_2^2}{2} [2\theta - \sin 2\theta] \end{aligned} \quad (\text{C.6})$$

where θ is determined from the following cosine law relationship

$$r_1^2 = h^2 + r_2^2 - 2hr_2 \cos \theta. \quad (\text{C.7})$$

Thus:

$$\theta = \cos^{-1} \left[\frac{h^2 + r_2^2 - r_1^2}{2hr_2} \right]. \quad (\text{C.8})$$

Similarly, the area of the sector S_4 is given by

$$\begin{aligned} S_4 &= \frac{1}{2} r_1 \gamma_1 - 2 \left[\frac{r_1 \cos \beta r_1 \sin \beta}{2} \right] \\ &= \frac{1}{2} r_1 (2r_1 \beta) - r_1^2 \sin \beta \cos \beta \\ &= \frac{r_1^2}{2} [2\beta - \sin 2\beta] \end{aligned} \quad (\text{C.9})$$

where

$$\begin{aligned} \beta &= \pi - \left(\pi - \sin^{-1} \left(\frac{r_2 \sin \theta}{r_1} \right) \right) \\ &= \sin^{-1} \left(\frac{r_2 (4h^2 r_2^2 - (h^2 + r_2^2 - r_1^2)^2)^{1/2}}{(2hr_2)} \right). \end{aligned} \quad (\text{C.10})$$

Then the area of overlap is given by

$$A = S_1 - 2(\pi r_1^2 - (S_4 - S_3)). \quad (\text{C.11})$$

The corresponding MAT is simply

$$K_\phi^3(h) = \frac{S_1 - 2(\pi r_1^2 - (S_4 - S_3))}{\pi(r_2^2 - r_1^2)}. \quad (\text{C.12})$$

4) For $r_2 \cos \theta \leq h < r_2 + r_1$: This corresponds to the situation where the shift h is greater than the first half of the inner circle but less than $r_2 + r_1$. In this case, the analysis is very similar to the previous one except that the two terms S_3 and S_5 will have different representations. This is illustrated in Figs. 12(e) and 13(b). The area of overlap is given by $A = S_1 - 2Y$. In this case the partial area Y is given by

$$Y = S_5 + S_3 \quad (\text{C.13})$$

where S_3 is the same as in (C.8). As seen from Fig. 13(b), the form of S_5 is basically the same as S_3 . That is:

$$S_5 = \frac{r_1}{2} (2\alpha - \sin 2\alpha). \quad (\text{C.14})$$

Note that in this case

$$\frac{\sin \alpha}{r_2} = \frac{\sin \theta}{r_1}. \quad (\text{C.15})$$

This implies that

$$\alpha = \sin^{-1} \left(\frac{r_2}{r_1} \sin \theta \right). \quad (\text{C.16})$$

Then the MAT is simply given by

$$K_\phi^3(h) = \frac{S_1 - 2(S_5 + S_3)}{\pi(r_2^2 - r_1^2)}. \quad (\text{C.17})$$

5) For $r_2 + r_1 \leq h < 2r_2$: The interaction of the annulus and its replica for this situation is depicted in Fig. 12(f). The area of overlap simply equals to S_1 and the corresponding MAT is

$$K_\phi^3(h) = \frac{S_1}{\pi(r_2^2 - r_1^2)}. \quad (\text{C.18})$$

When the spatial shift h is greater than $2r_2$, $K_\phi^3(h)$ diminishes. This completes the calculation of the MAT. In summary, the MAT is described by the following equation:

$$K_\phi^3(h) = \begin{cases} \frac{S_1 - (2\pi r_1^2 - S_2)}{\pi(r_2^2 - r_1^2)}, & 0 \leq h < 2r_1 \\ \frac{S_1 - 2\pi r_1^2}{\pi(r_2^2 - r_1^2)}, & 2r_1 \leq h < r_2 - r_1 \\ \frac{S_1 - 2(\pi r_1^2 - (S_4 - S_3))}{\pi(r_2^2 - r_1^2)}, & r_2 - r_1 \leq h < r_2 \cos \theta \\ \frac{S_1 - 2(S_5 + S_3)}{\pi(r_2^2 - r_1^2)}, & r_2 \cos \theta \leq h < r_2 + r_1 \\ \frac{S_1}{\pi(r_2^2 - r_1^2)}, & r_2 + r_1 \leq h < 2r_2 \\ 0, & 2r_2 \leq h \end{cases} \quad (\text{C.19})$$

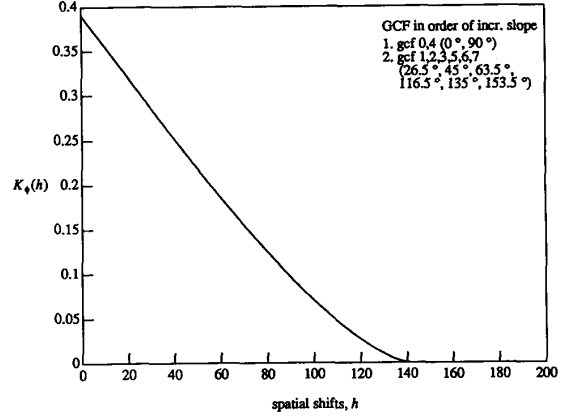


Fig. 14. MAT of the reference object "disk."

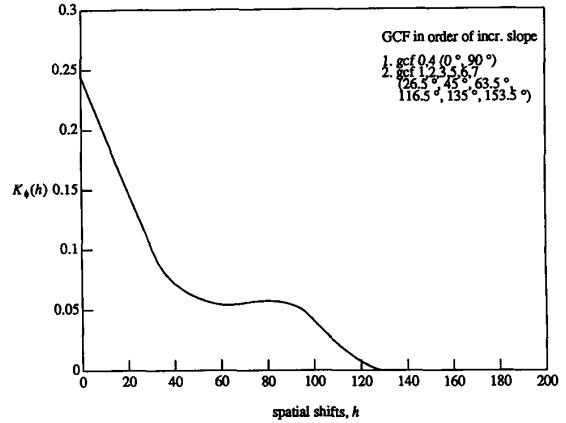


Fig. 15. MAT of the reference object "annulus."

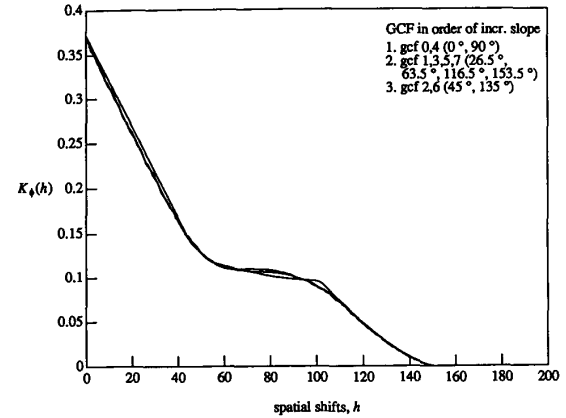


Fig. 16. MAT of the reference object "socket."

where S_1 , S_2 , S_3 , S_4 , S_5 , θ , β , and α are given by (C.2), (C.3), (C.6), (C.9), (C.14), (C.8), (C.10), and (C.16), respectively.

APPENDIX D

See Figs. 14–25.

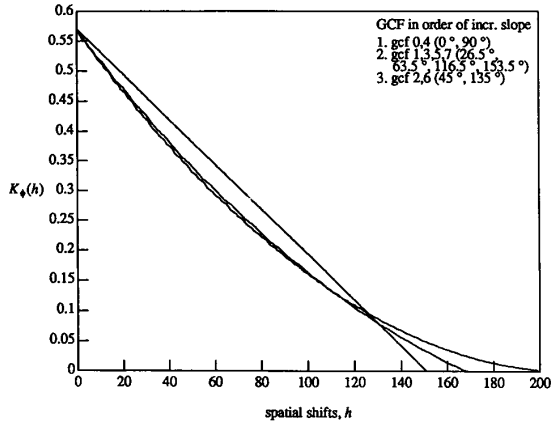


Fig. 17. MAT of the reference object "square."

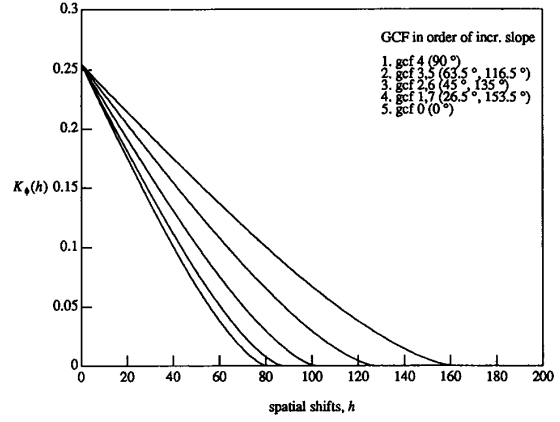


Fig. 20. MAT of the reference object "ellipse."

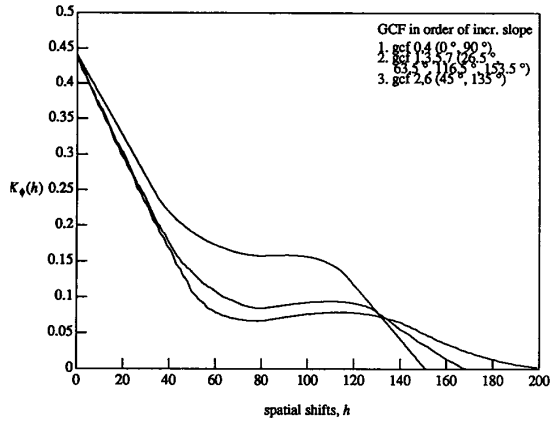


Fig. 18. MAT of the reference object "nut."

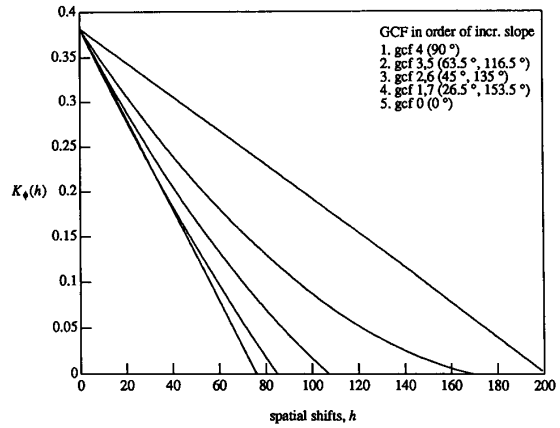


Fig. 21. MAT of the reference object "rectangle."

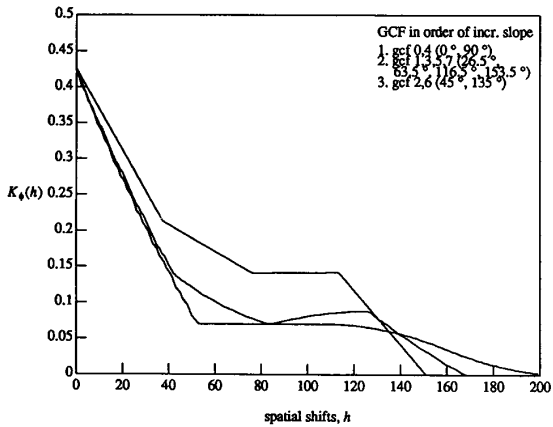


Fig. 19. MAT of the reference object "frame."

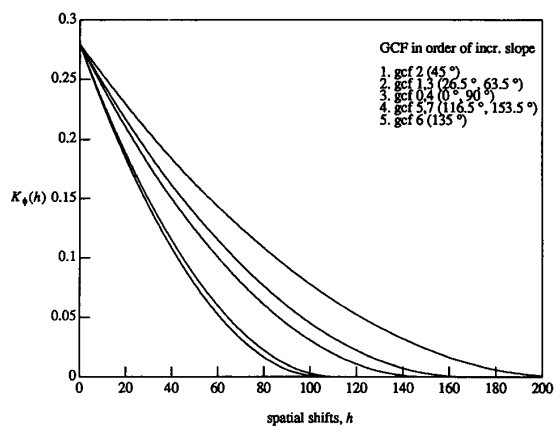


Fig. 22. MAT of the reference object "triangle."

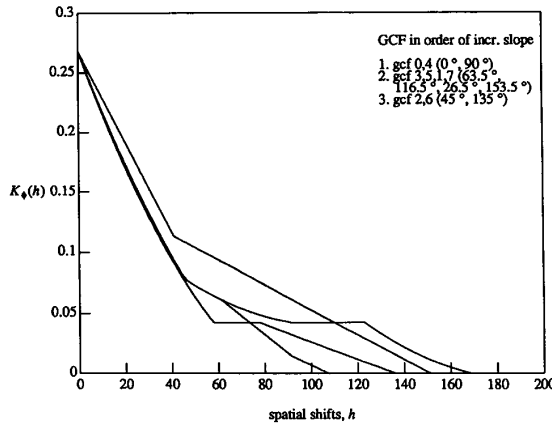


Fig. 23. MAT of the reference object "T."

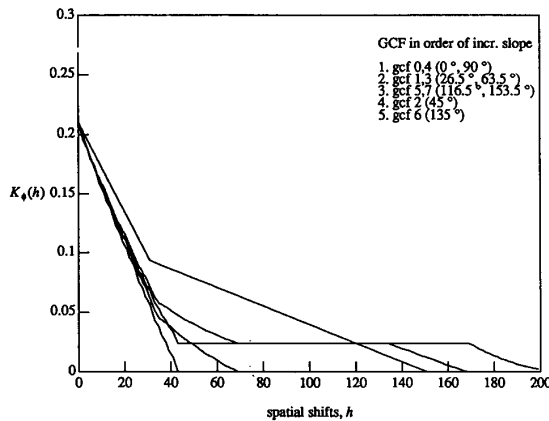


Fig. 24. MAT of the reference object "angle."

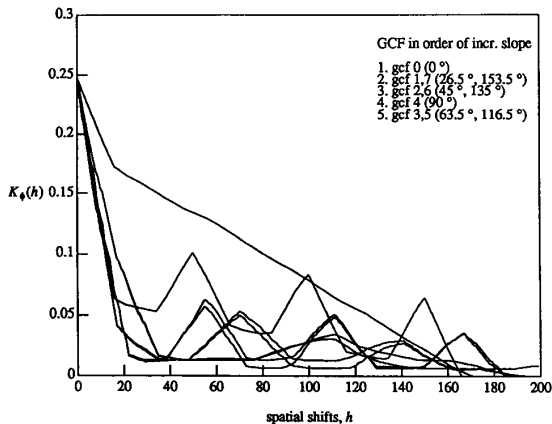


Fig. 25. MAT of the reference object "E."

REFERENCES

- [1] M. Levine, *Vision in Man and Machine*. New York: McGraw-Hill, 1985.
- [2] H. Freeman, "Computer processing of line drawing images," *Comput. Surv.*, vol. 6, no. 1, pp. 57-98, Mar. 1974.
- [3] E. Persoon and K. S. Fu, "Shape discrimination using Fourier descriptors," in *Proc. 2nd IJCP*, Aug. 1974, pp. 126-130.
- [4] R. C. Gonzalez and P. Wintz, *Digital Image Processing*, vol. 2. Reading, MA: Addison Wesley, 1987.
- [5] H. Freeman, "Shape description via the use of critical points," in *Proc. IEEE Computer Society Conf. on Pattern Recognition and Image Processing*, Troy, NY, June 6-8, 1977, pp. 168-174.
- [6] H. Samet, "Region representation: quadtrees from boundary codes," *Comm. ACM*, vol. 23, no. 3, pp. 163-170, Mar. 1980.
- [7] R. M. Haralick, S. R. Sternberg, and X. Zhuang, "Image analysis using mathematical morphology," *IEEE Trans. Pattern Anal. Mach. Intell.*, vol. PAMI-9, pp. 532-550, July 1987.
- [8] P. Maragos and R. W. Schafer, "Morphological filters—Part I: Their set-theoretic analysis and relations to linear shift-invariant filters," *IEEE Trans. Acoust., Speech, Signal Processing*, vol. ASSP-35, pp. 1153-1169, Aug. 1987.
- [9] R. L. Stevenson and G. R. Arce, "Morphological filters: statistics and further syntactic properties," *IEEE Trans. Circuits Syst.*, vol. CAS-34, Nov. 1987.
- [10] P. Maragos and R. W. Schafer, "Morphological skeleton representation and coding of binary images," *IEEE Trans. Acoust., Speech, Signal Processing*, vol. ASSP-34, pp. 1228-1244, Oct. 1986.
- [11] Z. Zhou and A. N. Venetsanopoulos, "Pseudo-euclidean morphological skeleton transform for machine vision," in *Proc. IEEE Int. Conf. on Acoustics, Speech and Signal Processing*, Glasgow, England, 1989.
- [12] J. F. Bronskill and A. N. Venetsanopoulos, "The pecstrum," in *Proc. 3rd ASSP Workshop on Spectral Estimation and Modelling*, Boston, 1986.
- [13] P. Maragos, "Pattern spectrum of images and morphological shape-size complexity," in *Proc. IEEE Int. Conf. on Acoustics, Speech and Signal Processing*, Dallas, TX, 1987, pp. 241-244.
- [14] I. Pitas and A. N. Venetsanopoulos, *Nonlinear Digital Filters—Principles and Applications*. Boston: Kluwer Academic, 1990.
- [15] J. Serra, *Image Analysis and Mathematical Morphology*. New York: Academic, 1982.
- [16] A. C. P. Loui, "A morphological approach to moving-object recognition with applications to machine vision," Ph.D. dissertation, Dep. Elec. Eng. Univ. of Toronto, Toronto, Canada, Sept. 1990.
- [17] A. C. P. Loui, A. N. Venetsanopoulos, and K. C. Smith, "Two-dimensional shape representation using morphological correlation functions," in *Proc. IEEE Int. Conf. Acoustics, Speech and Signal Processing*, Albuquerque, NM, Apr. 3-6, 1990, pp. 2165-2168.
- [18] G. Matheron, *Random Set and Integral Geometry*. New York: Wiley, 1970.
- [19] A. C. P. Loui, A. N. Venetsanopoulos, and K. C. Smith, "Flexible architectures for morphological signal processing and analysis," *IEEE Trans. Circuits Syst. Video Technol.*, Mar. 1992.



Alexander C. P. Loui (S'82-M'90) received the B.A.Sc., M.A.Sc., and Ph.D. degrees in electrical engineering, all from the University of Toronto, Toronto, Canada in 1983, 1986, and 1990, respectively.

From 1986 to 1990, he was Research Assistant of the Signal Processing Laboratory at the Department of Electrical Engineering, University of Toronto. In 1990 he joined Bell Communications Research, Red Banks, NJ, as a Member of Technical Staff. His current research interests include video signal processing, high-speed architectures, image processing, and computer vision.



Anastasios N. Venetsanopoulos (S'66-M'69-SM'79-F'88) received the B.S. degree from the National Technical University of Athens (NTU), Greece, in 1965, and the M.S., M.Phil., and Ph.D. degrees in electrical engineering, all from Yale University, in 1966, 1968, and 1969, respectively.

He joined the University of Toronto, Canada, in 1968, where he is now a Professor in the Department of Electrical Engineering. He also served as Chairman of the Communications Group (1974-

1978 and 1981-1986), and as Associate Chairman of the Department of Electrical Engineering (1978-1979). He was on research leave at the Swiss Federal Institute of Technology, the University of Florence, the Federal University of Rio de Janeiro, the National Technical University of Athens, and the Imperial College of Science and Technology, and was Adjunct Professor at Concordia University. He served as Lecturer of numerous short courses to industry and continuing education programs; he is a contributor to eleven books and has published over 300 papers in digital signal and image processing, and digital communications; he also served as consultant to several organizations, and as Editor of the *Canadian Electrical Engineering Journal* (1981-1983).

Dr. Venetsanopoulos has served the IEEE in the following capacities. *IEEE Activities-Boards*: IEEE Educational Activities Board (1987). *Regions*: Region 7, Educational Activities Committee Chairman (1986), Nominations and Appointments Committee (1982). *Councils*: Central Canada Council; Chairman (1981-1982), Past Chairman and Nominations Committee Chairman (1983-1984). *Sections*: Toronto; Chairman (1977-1979), Vice Chairman (1976-1977), Educational Activities Coordinator (1974-1976), Past Chairman and Nominations Committee Chairman (1979-1981). *Societies*: Circuits and Systems: Associate Editor in Digital Signal Processing, IEEE TRANSACTIONS ON CIRCUITS AND SYSTEMS (1985-1987); Guest Editor, Special Issue on Digital Image Processing and Applications, IEEE TRANSACTIONS ON CIRCUITS AND SYSTEMS (November 1987). *Conferences*: Canadian Communications and Energy Conference, Program Committee (1978, 1982). Electronicon, Program Committee (1971, 1973, 1975, 1983, 1985). International Conference on Communications, Program Chairman (1978, 1986). International Symposium on Circuits and Systems, Finance Chairman (1983). International Conference on Acoustics, Speech, and Signal Processing, Program Chairman (1991). *Representative*: IEEE/CSEE Joint Committee, Region 7 (1983-1984). He was President of the Canadian Society for Electrical Engineering and Vice-President of the Engineering Institute of Canada (1983-1984). He was a Fulbright Scholar, A. F. Schmitt Scholar, and recipient of the J. Vakis Award. He is a member of the New York Academy of Sciences, Sigma Xi, the International Society for Optical Engineering, and the Technical Chamber of Greece; he is a Registered Professional Engineer in Ontario and Greece, and a Fellow of the Engineering Institute of Canada.



Kenneth Carless Smith (S'53-M'60-SM'76-F'78) was born in Toronto, Canada, on May 8, 1932. He received the B.A.Sc. degree in engineering physics in 1954, the M.A.Sc. degree in electrical engineering in 1956, and the Ph.D. degree in physics in 1960, all from the University of Toronto, Toronto, Canada.

From 1954 to 1955 he served with Canadian National Telegraphs as a Transmission Engineer. In 1956 he joined the Computation Centre, University of Toronto, as a Research Engineer assigned to assist in the development of high-speed computers at the Digital Computer Laboratory, University of Illinois, Urbana. In 1960 he joined the staff of the Department of Electrical Engineering at the University of Toronto as an Assistant Professor. In 1961 he returned to the University of Illinois as Assistant Professor of Electrical Engineering where he became Chief Engineer of Illiac II, and then of Illiac III, and attained the rank of Associate Professor of Computer Science. In 1965 he returned to Toronto, where he is currently a Professor in the Departments of Electrical Engineering, Mechanical Engineering, Computer Science, and Information Science, and was Chairman of the Department of Electrical Engineering from 1976 to 1981. His research interests include analog, multiple-valued, and binary circuit and systems design, instrumentation in manufacturing, and computer architectures emphasizing parallelism and reliability. He is the co-author with A. S. Sedra of *Microelectronic Circuits* (HRW/Saunders College). He is also an advisor to several international companies in the area of new-product development and education.

Dr. Smith has participated widely in technical and professional organizations, including the Canadian Society for Electrical Engineers (CSEE) and the Canadian Society for Professional Engineers (CSPE) including, since 1974, membership on the Executive Committee of the International Solid-State Circuits Conference (ISSCC) as Awards Chairman, and in other roles. As well as being on the Technical Committee on Multiple-Valued Logic of the Computer Society of the IEEE, he is the Vice-Chair for Technical Activities and Co-Program Chair of ISMVL 92 in Sendai, Japan. Since 1988, he has been President of CSPE.